Ultra-broadband chirped-pulse optical parametric amplifier with angularly dispersed beams

Gunnar Arisholm
Forsvarets forskningsinstitutt (Norwegian Defence Research Establishment), Postboks 25, NO-2027 Kjeller, Norway
gunnar.arisholm@ffi.no

Jens Biegert, Philip Schlup, Christoph P. Hauri, and Ursula Keller
Physics Department, Institute of Quantum Electronics, Swiss Federal Institute of Technology, ETH Hönggerberg, CH-8093 Zürich, Switzerland
biegert@phys.ethz.ch

Abstract: We propose a BBO-based chirped-pulse optical parametric amplifier employing an angularly dispersed signal beam to yield a full-octave gain bandwidth, sufficient for the direct amplification of sub-10-fs pulses. Numerical simulations show that this power-scalable amplifier configuration has a small-signal gain of 10^7 at a pumping intensity of 45 GW/cm^2. The additional phase-matching flexibility compared to alternative configurations permits the suppression of parasitic second harmonic generation of the signal beam.

OCIS codes: (190.4970) Parametric oscillators and amplifiers; (320.1590) Chirping; (190.7110) Ultrafast nonlinear optics; (140.4480) Optical amplifiers; (190.4410) Nonlinear optics, parametric processes

References and links

1. S. Backus, C.G. Durfee, M.M. Murnane, and H.C. Kapteyn, "High power ultrafast lasers," Rev. Sci. Instrum. **69**, 1207-1223 (1998).
2. M. Zavelani-Rossi, F. Lindner, C. Le Blanc, G. Cheriaux, and J.P. Chambaret, "Control of thermal effects for high-intensity Ti:sapphire laser chains," Appl. Phys. B **70**, S193-S196 (2000).
3. S. Sartania, Z. Cheng, M. Lenzner, G. Tempea, C. Spielmann, F. Krausz, and K. Ferencz, "Generation of 0.1-TW 5-fs optical pulses at a 1-kHz repetition rate," Opt. Lett. **22**, 1562-1564 (1997).
4. J. Seres, A. Müller, E. Seres, K. O'Keeffe, M. Lenner, R.F. Herzog, D. Kaplan, C. Spielmann, and F. Krausz, "Sub-10-fs, terawatt-scale Ti:sapphire laser system," Opt. Lett. **28**, 1832-1834 (2003).
5. C.P. Hauri, M. Bruck, W. Kornelis, J. Biegert and U. Keller, "Generation of 14.8-fs pulses in a spatially dispersed amplifier," Opt. Lett. **29**, 201-203 (2004).
6. G. Cerullo, M. Nisoli, S. Stagira, and S. De Silvestri, "Sub-8-fs pulses from an ultra-broadband optical parametric amplifier in the visible," Opt. Lett. **23**, 1283-1285 (1998).
7. A. Shirakawa, I. Sakane, and T. Kobayashi, "Pulse-front-matched optical parametric amplification for sub-10-fs pulse generation tunable in the visible and near infrared," Opt. Lett. **23**, 1292-1294 (1998).
8. A. Baltuska, T. Fuji, and T. Kobayashi. "Visible pulse compression to 4 fs by optical parametric amplification and programmable dispersion control," Opt. Lett. **27**, 306-308 (2002).
9. E. Riedle, M. Beutter, S. Lochbrunner, J. Piel, S. Schenkl, S. Spörlöein, and W. Zinth, "Generation of 10 to 50 fs pulses tunable through all of the visible and the NIR," Appl. Phys. B **71**, 457-465 (2000).
10. A. Dubietis, G. Jonusauskas, and A. Piskarskas, "Powerful femtosecond pulse generation by chirped and stretched pulse parametric amplification in BBO crystal," Opt. Commun. **88**, 437-440 (1992).

#3504 - $15.00 US Received 10 December 2003; revised 3 February 2004; accepted 3 February 2004

11. I.N. Ross, P. Matousek, M. Towrie, A.J. Langley, and J.L. Collier, "The prospects for ultrashort pulse duration and ultrahigh intensity using optical parametric chirped pulse amplifiers," Opt. Commun. **144**, 125-133 (1997).
12. X. Yang, Z. Xu, Y. Leng, H. Lu, L. Lin, Z. Zhang, R. Li, W. Zhang, D. Yin, and B. Tang, "Multiterawatt laser system based on optical parametric chirped pulse amplification," Opt. Lett. **27**, 1135-1137 (2002).
13. I.N. Ross, J. Collier, P. Matousek, C.N. Danson, N. Neely, R.M. Allott, D.A. Pepler, C. Hernandez-Gomez, and K. Osvay, "Generation of terawatt pulses by use of optical parametric chirped pulse amplification," Appl. Opt. **39**, 2422-2427 (2000).
14. I. Jovanovic, C.A. Ebbers, B.C. Stuart, M.R. Hermann, and E.C. Morse, "Nondegenerate optical parametric chirped pulse amplification," in *Conference on Lasers and Electro-Optics* , Vol. 73 of Trends in Optics and Photonics , (Optical Society of America, Washington DC, 2002), pp. 387–388.
15. P. Di Trapani, A. Andreoni, C. Solcia, P. Foggi, R. Danielius, A. Dubietis, and A. Piskarskas, "Matching of group velocities in three-wave parametric interaction with femtosecond pulses and application to traveling-wave generators," J. Opt. Soc. Am. B **12**, 2237-2244 (1995).
16. V.D. Volosov, S.G. Karpenko, N.E. Kornienko, and V.L. Strizhevskii, "Method for compensating the phase-matching dispersion in nonlinear optics," Sov. J. Quantum Electron. **4**, 1090-1098 (1975).
17. O.E. Martinez, "Achromatic phase matching for second harmonic generation of femtosecond pulses," IEEE J. Quantum Electron. **25**, 2464-2468 (1989).
18. G. Szabo and Z. Bor, "Broadband frequency doubler for femtosecond pulses," Appl. Phys. B **50**, 51-54 (1990).
19. T.R. Zhang, H.R. Choo, and M.C. Downer, "Phase and group velocity matching for second harmonic generation of femtosecond pulses," Appl. Opt. **29**, 3927-3933 (1990).
20. A.V. Smith, "Group-velocity-matched three-wave mixing in birefringent crystals," Opt. Lett. **26**, 719-721 (2001).
21. J. Piel, M. Beutter, and E. Riedle, "20–50-fs pulses tunable across the near infrared from a blue-pumped noncollinear parametric amplifier," Opt. Lett. **25**, 180-182 (2000).
22. K. Kato, "Second-harmonic generation to 2048 Å in β-BaB_2O_4," IEEE J. Quantum Electron. **22**, 1013-1014 (1986).
23. G.M. Gale, M. Cavallari, T.J. Driscoll, and F. Hache, "Sub-20-fs tunable pulses in the visible from an 82-MHz optical parametric oscillator," Opt. Lett. **20**, 1562-1564 (1995).
24. W.J. Alford and A.V. Smith, "Wavelength variation of the second-order nonlinear coefficients of $KNbO_3$, $KTiOPO_4$, $KTiOAsO_4$, $LiNbO_3$, $LiIO_3$, β-BaB_2O_4, KH_2PO_4, and LiB_3O_5 crystals: A test of Miller wavelength scaling," J. Opt. Soc. Am. B **19**, 524-533 (2001).
25. J. Biegert, P. Schlup, C.P. Hauri, U. Keller and G. Arisholm, "Design of a sub-13-fs, multi-gigawatt chirped pulse optical parametric amplification system," to be published, (2004).
26. G. Arisholm. "General numerical methods for simulating second order nonlinear interactions in birefringent media," J. Opt. Soc. Am. B **14**, 2543-2549 (1997).
27. G. Arisholm, "Quantum noise initiation and macroscopic fluctuations in optical parametric oscillators," J. Opt. Soc. Am. B **16**, 117-127 (1999).
28. J. Biegert and J.C. Diels, "Compression of pulses of a few optical cycles through harmonic generation," J. Opt. Soc. Am. B **18**, 1218-1226 (2001).
29. F. Verluise, V. Laude, J.-P. Huignard, P. Tournois, and A. Migus, "Arbitrary dispersion control of ultrashort optical pulses with acoustic waves," J. Opt. Soc. Am. B **17**, 138-145 (2000).
30. B. Schenkel, J. Biegert, U. Keller, C. Vozzi, M. Nisoli, G. Sansone, S. Stagira, S. De Silvestri, and O. Svelto, "Generation of 3.8-fs pulses from adaptive compression of a cascaded hollow fiber supercontinuum," Opt. Lett. **28**, 1987-1989 (2003).
31. R. DeSalvo, A.A. Said, D.J. Hagan, E.W. van Stryland, and M. Sheik-Bahae, "Infrared to ultraviolet measurements of two-photon absorption and n_2 in wide bandgap solids," IEEE J. Quantum Electron. **32**, 1324-1333 (1996).
32. M. Sheik-Bahae and M. Ebrahimzadeh, "Measurements of nonlinear refraction in the second-order $\chi^{(2)}$ materials $KTiOPO_4$, $KNbO_3$, β-BaB_2O_4, and LiB_3O_5," Opt. Commun. **142**, 294-298 (1997).

1. Introduction

Chirped-pulse optical parametric amplifiers (CPOPAs) are increasingly showing promise as alternatives to chirped-pulse amplifier systems based on e.g. Ti:sapphire, which suffer from gain narrowing [1] and thermal problems at high average powers unless they are cryogenically cooled [2]. The large gain bandwidths of CPOPAs potentially allow the direct amplification of sub-10 fs pulses, which are traditionally generated by spectral broadening in hollow fibers after the amplifier [3] or by spectral filtering between the amplifier stages [4]. Gain narrowing has also been overcome by using a spatially dispersed seed beam and tailoring the pump spatial distribution to selectively amplify the spectral wings [5]. These techniques lead to complex

#3504 - $15.00 US Received 10 December 2003; revised 3 February 2004; accepted 3 February 2004

system architectures and potentially reduce the amplification efficiency, and the output energy is ultimately limited by material absorption. By contrast, optical parametric amplifiers have negligible thermal loads, high gain, potentially large bandwidths, and are scalable in terms of peak and average power. They have already proven useful for ultra-broadband amplification of pulses at the μJ energy level, both in the visible and in the near-IR [6–9]. Chirped pulse OPAs (CPOPAs) [10, 11] have reached terawatt power levels for 1 μm pulses in the 100 fs regime [12, 13]. The CPOPA technique has also been applied in the wavelength range around 800 nm [14], but the reported 60 fs pulse duration did not exploit the full potential of the technique. The tilting of pulse fronts, which is equivalent to angularly dispersing the beam (this is explained in Section 3), has been exploited to match the group velocities of the pump and signal beams in OPAs [7, 15], and to increase the bandwidth with achromatic phase matching in second harmonic generation (SHG) [16–19]. Group velocity matching of all beams in a general three-wave interaction using pulse front tilting has been studied theoretically [20]. In chirped-pulse amplifier systems, the pulses are relatively long and matching the group velocity of the pump is not of primary importance, so that the angular dispersion can be chosen to optimize the amplifier gain bandwidth. We are not aware of a detailed investigation of this technique applied to CPOPAs.

In this paper we report a numerical study of a β-BaB_2O_4 (BBO)-based CPOPA, with angularly dispersed signal and idler beams to optimize the gain bandwidth. Our results show that it is possible to achieve a small-signal gain of $> 10^7$ and a full-octave bandwidth with realistic system parameters. An additional advantage of our configuration is that it does not suffer from phase-matched parasitic SHG, which can be a problem in other BBO-based OPAs [21]. The conditions for wide-band phase matching in BBO are formulated in Section 2, while a brief overview of tilted pulse and phase fronts and our choice of modeling configurations are given in Section 3. Our simulation results are presented in Section 4, and we draw conclusions in Section 5.

2. Wide-band phase matching

Energy conservation of a general three-wave interaction dictates that the angular frequencies ω_j satisfy

$$\omega_3 = \omega_2 + \omega_1, \tag{1}$$

where we define the indices $j = 3$, 2, and 1 to refer to the OPA pump, signal / seed, and idler, respectively. To first order, the frequency acceptance bandwidth of the nonlinear interaction with respect to the signal frequency is determined by $\mathrm{d}\Delta\mathbf{k}/\mathrm{d}\omega_2$, where $\Delta\mathbf{k} = \mathbf{k}_3 - \mathbf{k}_2 - \mathbf{k}_1$ is the phase mismatch. We adopt the definition of the wave vectors $\mathbf{k}$ being orthogonal to the phase fronts with magnitude $k(\omega) = \omega n(\omega)/c$, where $n(\omega)$ is the (dispersive) refractive index and c the vacuum velocity of light, and employ the Sellmeier equations of Kato [22], which are based on measurements between 205 nm and 1064 nm. For a quasi-monochromatic pump, ω_3 is constant, and the signal acceptance bandwidth is given by

$$\frac{\mathrm{d}\Delta\mathbf{k}}{\mathrm{d}\omega_2} = -\frac{\mathrm{d}\mathbf{k}_2}{\mathrm{d}\omega_2} - \frac{\mathrm{d}\mathbf{k}_1}{\mathrm{d}\omega_2} = -\frac{\mathrm{d}\mathbf{k}_2}{\mathrm{d}\omega_2} + \frac{\mathrm{d}\mathbf{k}_1}{\mathrm{d}\omega_1}. \tag{2}$$

When this derivative vanishes, i.e. when the group velocities $\mathrm{d}k_j/\mathrm{d}\omega_j$ of the signal and idler are equal, the bandwidth becomes large, with the actual value being determined by higher order derivatives.

As an example, it is well known that the bandwidth is large in degenerate collinear type 1 interactions. In this case, the signal and idler beams are identical with equal group velocities. However, the equivalence of signal and idler beams makes this configuration phase-sensitive and therefore not practical for broadband amplifiers. In a collinear phase matching geometry,

#3504 - $15.00 US Received 10 December 2003; revised 3 February 2004; accepted 3 February 2004

the crystal orientation is selected to satisfy the phase matching conditions, and the crystal length to yield the desired gain, leaving no further design parameters to optimize the gain bandwidth. Noncollinear phase matching gives much greater scope for tailoring the bandwidth.

Although our simulation model is general, in the following examples we restrict our attention to noncollinear interactions in the **YZ** crystal plane of BBO, where **Z** is the crystal optic axis, as shown in Fig. 1. The phase matching angle θ is defined as the polar angle between the optic axis **Z** and the pump propagation vector $\mathbf{k}_3$. We denote the noncollinear angle between $\mathbf{k}_2$ and $\mathbf{k}_3$ by α. In addition to the crystal axes **X**, **Y**, and **Z**, we use a model coordinate system with axes $\hat{\mathbf{x}}$, $\hat{\mathbf{y}}$, and $\hat{\mathbf{z}}$, where $\hat{\mathbf{z}}$ is parallel to the pump beam and the model $\hat{\mathbf{x}}$ axis lies in the crystal **YZ** plane. We take the crystal to be cut so that its face is perpendicular to the pump beam (and $\hat{\mathbf{z}}$ axis). This choice has the advantage that, because of Snell's law, the transverse components of a wave vector, k_x and k_y, remain constant across the crystal interface.

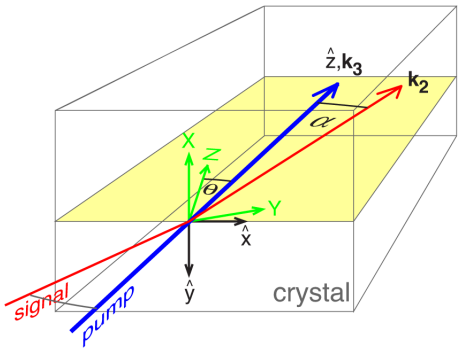

Fig. 1. Crystal axes **X**, **Y**, **Z** (green) and model axes $\hat{\mathbf{x}}$, $\hat{\mathbf{y}}$, $\hat{\mathbf{z}}$ (black). The pump wave vector $\mathbf{k}_3$ is perpendicular to the crystal face and parallel to $\hat{\mathbf{z}}$. $\mathbf{k}_2$ (red) is the signal wave vector with internal noncollinear angle α.

The features of noncollinear phase matching in BBO can be explained by aid of Fig. 2. The figure shows the loci of noncollinear angles α, for different phase matching angles θ, for which phase matching is satisfied. Perfect phase matching with an angularly dispersed signal beam could be achieved across the entire bandwidth if $\alpha(\omega)$ at each seed frequency ω could be made to follow one of the curves. Creating such an arbitrary angular dispersion is difficult, so we focus our attention to two forms of noncollinear phase matching: a collimated signal beam tilted with respect to the pump beam (horizontal lines in Fig. 2); and a signal beam additionally dispersed by a diffraction grating (lines of constant slope).

3. Pulse-front tilting

The numerical simulation uses a transverse wavenumber $k_x(\omega)$ representation for each frequency component to efficiently handle tilted beams, wave-, and pulse-fronts. The transverse wavenumber and noncollinear angle $\alpha(\omega)$ are geometrically related by $\sin[\alpha(\omega)] = k_x(\omega)/|\mathbf{k}(\omega)|$. Because of our choice of coordinate system and crystal cut, k_x is the same inside and outside the crystal, although the noncollinear angle is changed by refraction.

Figure 3(a) shows the **k** vectors for the central frequency (black) as well as two extreme frequencies components (blue, red) in the case of a collimated signal beam. Tilting the entire beam relative to the pump vector yields a noncollinear angle α that is constant for all frequencies. Phase matching results in a dispersed idler even though the seed beam is collimated. A constant α corresponds to a horizontal line in Fig. 2; when such a line is tangent to a phase matching curve, $\Delta\mathbf{k}$ becomes independent of wavelength to first order (matched group veloc-

#3504 - $15.00 US Received 10 December 2003; revised 3 February 2004; accepted 3 February 2004

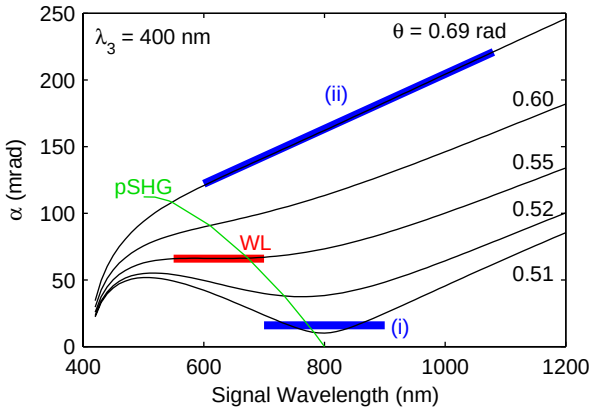

Fig. 2. Phase-matching curves for noncollinear type 1 (*ooe*) interactions in BBO with a pump wavelength of 400 nm. Each black curve shows the loci of perfect phase matching ($\Delta\mathbf{k} = 0$) for a specific value of θ, while the green line shows wavelengths at which parasitic second harmonic generation is phase matched. The broadband phase matching configuration that has previously been used for white-light seeded OPAs is shown in red (WL). The configurations marked in blue are investigated in this paper.

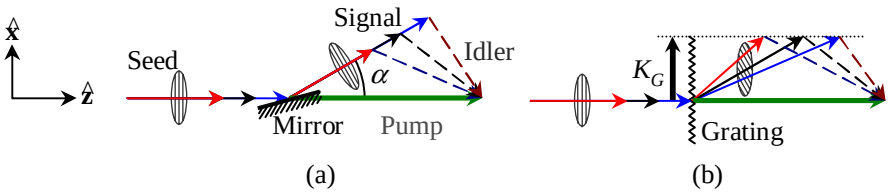

Fig. 3. (a) Tilted collimated beam and (b) angularly dispersed beam in model $\hat{\mathbf{x}}\hat{\mathbf{z}}$ plane. (a) The seed beam (solid lines) is tilted by noncollinear angle α, constant for all wavelengths (blue, red), and interacts with a monochromatic pump (green) to yield a dispersed idler (dashed). (b) Influence of diffraction grating adding constant K_G to all frequency components, resulting in a tilted pulse relative to the central $\mathbf{k}$ (black). K_G is the grating vector.

ities for signal and idler) and gives a broad gain bandwidth. When a phase matching curve is approximately horizontal over an extended range of wavelengths, the second order derivative of the phase mismatch is also small and good phase matching can be achieved across the whole range. One such configuration, which has been exploited in many experiments [6, 7, 23], is the flat section between 550 nm and 700 nm (red line in Fig. 2) for $\theta = 0.55\,\text{rad}$ and $\alpha = 66\,\text{mrad}$ (3.7°).

Figure 3(b) shows the influence of diffraction off a grating in the $\hat{\mathbf{x}}$ axis. Mathematically, a grating with groove spacing Λ multiplies the pulse envelope by $\exp(iK_G x)$, where the grating vector $K_G = 2\pi/\Lambda$, which is equivalent to imposing a constant transverse wave vector component K_G on all frequency components. The pulse front (which is determined by the intensity distribution) is not affected, resulting in a signal with a pulse front tilted relative to the central beam direction (black). The frequency-dependent noncollinear angle in the crystal can be written as $\alpha(\omega) = \sin^{-1}(\lambda/(n\Lambda)) \approx \lambda/(n\Lambda)$ for small diffraction angles. The equivalence of angular dispersion and a tilted pulse front is illustrated in Fig. 4. Phase matching results in all idler components having transverse wave vector components of $k_x = -K_G$, and, in the general case, both the signal and idler beams are angularly dispersed.

#3504 - $15.00 US Received 10 December 2003; revised 3 February 2004; accepted 3 February 2004

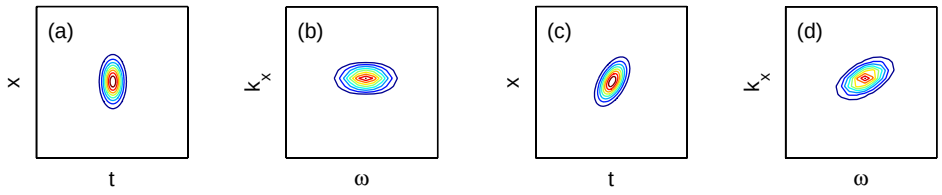

Fig. 4. Equivalence of angular dispersion and pulse tilt. (a) Untilted pulse envelope, $\mathscr{E}(x,t)$, where $\hat{\mathbf{x}}$ is normal to the propagation direction. (b) Fourier transform $\tilde{E}(k_x,\omega) = \int\int \mathscr{E}(x,t)\exp(i(\omega t - k_x x))\,\mathrm{d}x\,\mathrm{d}t$. (c) Tilted pulse $\mathscr{E}'(x,t) = \mathscr{E}(ax - bct, at + bx/c)$, where c is the velocity of light and a and b are rotation coefficients that satisfy $a^2 + b^2 = 1$. (d) Fourier transform of the tilted pulse, which can be shown to be $\tilde{E}'(k_x,\omega) = \tilde{E}(ak_x + b\omega/c, a\omega - bck_x)$. The angular dispersion is reflected by the variation of k_x with ω.

The approximately linear relation between α and λ means that beams tilted and dispersed by a grating correspond to straight sloping lines in Fig. 2. A suitable combination of beam tilt and grating dispersion can thus be chosen to phase match a wavelength range over which the phase matching curve has a constant slope. Since the curves in Fig. 2 have constant slopes that cover much wider and more diverse wavelength ranges than the horizontal sections, angular dispersion offers greater flexibility in phase matching broadband beams. The approximate relation between α and λ can only be used to identify potential broadband phase matching configurations; in the final phase matching calculations below we use the exact relation for k_x. For an angularly dispersed beam with fixed k_x, the projection of the group velocity onto the $\hat{\mathbf{z}}$-direction is given by

$$v_{g,z} = \left(\frac{\mathrm{d}k_z}{\mathrm{d}\omega}\right)^{-1} = v_g \cos[\alpha(\omega)], \tag{3}$$

where v_g is the group velocity parallel to $\mathbf{k}$.

Although the phase mismatch is the most important factor determining the bandwidth, it is necessary to calculate the actual gain to analyze an interaction in detail. The small-signal gain coefficient g in the presence of a phase mismatch Δk is given by

$$g = \sqrt{\gamma^2 \omega_1 \omega_2 I_3 - \left(\frac{\Delta k}{2}\right)^2}, \tag{4}$$

where

$$\gamma = \frac{\chi_{\mathrm{eff}}}{c}\sqrt{\frac{Z_0}{2n_1 n_2 n_3}}, \tag{5}$$

$\chi_{\mathrm{eff}} = 2d_{\mathrm{eff}}$ is the effective nonlinear susceptibility, and Z_0 is the vacuum impedance. Equation (4) shows that the tolerance to phase mismatch increases with gain and can be estimated by $|\Delta k| \lesssim g_0$, where g_0 is the gain coefficient in the absence of phase mismatch. Furthermore, the gain depends on frequency through the factor $(\omega_2\omega_1)^{1/2} = [\omega_2(\omega_3 - \omega_2)]^{1/2}$, which, for a fixed range of variation for ω_2, varies least if the center frequency equals $\omega_3/2$.

We are interested in broadband amplification around 800 nm with a 400 nm pump, so we identify two potential configurations marked in Fig. 2: (i) $\theta = 0.51\,\mathrm{rad}$ and $\alpha = 16\,\mathrm{mrad}$ with a collimated signal beam; and (ii) $\theta = 0.69\,\mathrm{rad}$ and angular dispersion with $k_x = 2106\,\mathrm{mm}^{-1}$ (k_x has the same value inside and outside the crystal, as explained above). Other configurations are also possible, but these two were found to give maximum bandwidth for the cases

#3504 - $15.00 US Received 10 December 2003; revised 3 February 2004; accepted 3 February 2004

with collimated and angularly dispersed signals, respectively. For type 1 phase matching in BBO, propagation in the **YZ** plane gives the maximum nonlinear coefficient, $d_{\text{eff}} = d_{yxx}\cos\theta$. $|d_{yxx}| = |d_{yyy}|$ because of Kleinman symmetry, and $d_{yyy} = 2.2\,\text{pm/V}$ [24]. For the gain calculations we take a pump intensity of 45 GW/cm^2, which gives g_0 in the range 3.5–4.1 mm^{-1} for our configurations. To get comparable results we adjust the crystal length L_c to obtain a peak gain of about 10^8 in each case. We analyzed these configurations by plotting the phase mismatch $\Delta k = |\Delta\mathbf{k}|\text{sign}(\Delta\mathbf{k}\cdot\mathbf{k}_3)$ and small-signal gain g as functions of frequency, and optimized them by fine-tuning the crystal orientation and noncollinear parameters. The results are shown in Figs. 5 and 6.

For case (i) (Fig. 5), the central 800 nm wavelength is phase matched with a noncollinear angle of $\alpha = 10\,\text{mrad}$ (black line). Increasing the noncollinear angle to $\alpha = 16\,\text{mrad}$ (red) gives a greater gain bandwidth, as can be seen in Fig. 5(b); but increasing α further to 22 mrad (green) results in a significant dip of the gain at the center frequency. Detailed simulations of this configuration were recently reported for a CPOPA system based on measured 12 fs seed pulses [25].

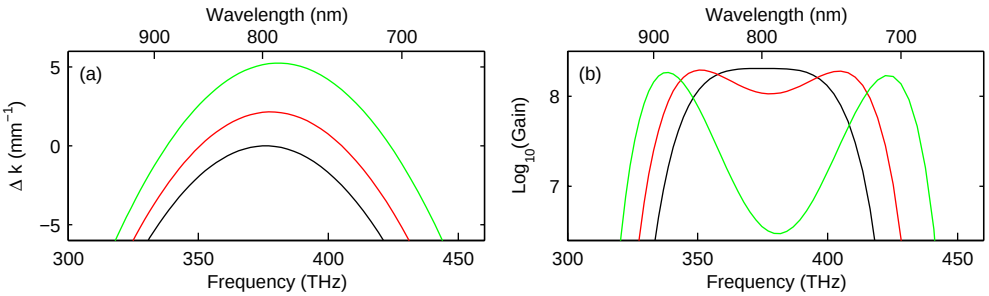

Fig. 5. (a) Phase mismatch Δk; and (b) gain; as functions of signal frequency ω_2 for $\lambda_3 = 400\,\text{nm}$, $\theta = 0.51$, and $L_c = 2.5\,\text{mm}$. $\alpha = 10\,\text{mrad}$ (black), $\alpha = 16.2\,\text{mrad}$ (red), and $\alpha = 22.3\,\text{mrad}$ (green).

In configuration (ii), k_x is constant, so α is approximately proportional to λ. Since the signal and idler have the same polarization, opposite k_x, and both are centered at the degenerate wavelength, there is a complete symmetry between the two. Figure 6 shows the phase mismatch and gain for two different values for k_x. With $k_x = 2106\,\text{mm}^{-1}$ (black curve), we find a bandwidth from 600 to 1200 nm, constant to within half an order of magnitude. The central peak is due to the frequency factor in the gain coefficient. The gain curve can be flattened by changing the phase mismatch to $k_x = 2110\,\text{mm}^{-1}$ (red), but this reduces the bandwidth slightly, as seen in Fig. 6 (b). These k_x dispersions correspond to diffraction off gratings with around 330 lines per mm.

An additional flexibility provided by phase matching with a dispersed seed beam is the suppression of parasitic SHG of the signal, which has been observed in other type 1 phase-matched BBO-based broadband OPAs [21]. The phase matching angles for collinear SHG in BBO at wavelengths of interest to the configurations investigated here are shown by the green line in Fig. 2. In the simple noncollinear phase matching of case (i), parasitic SHG at around 800 nm is phase matched and could potentially distort the amplified spectrum and reduce the conversion efficiency. By contrast, in configuration (ii) with $\theta \approx 0.7\,\text{rad}$, phase matched SHG is possible only for wavelengths shorter than 600 nm, which lie outside the gain bandwidth (see Fig. 6). In general wide-band OPAs, parasitic sum frequency generation (SFG) of different signal fre-

#3504 - $15.00 US Received 10 December 2003; revised 3 February 2004; accepted 3 February 2004

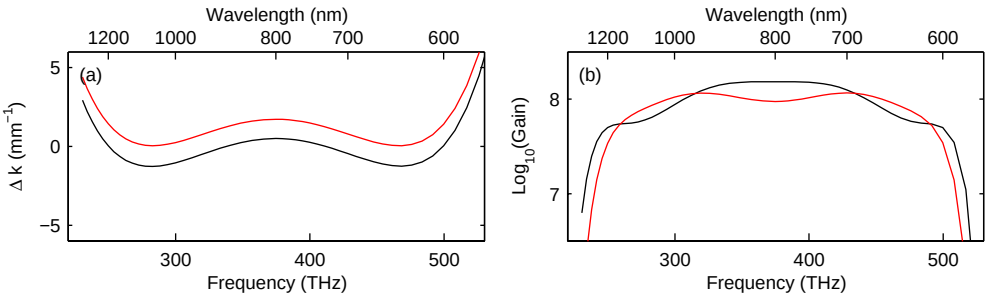

Fig. 6. (a) Phase mismatch and (b) gain as functions of signal frequency for $\lambda_3 = 400\,\text{nm}$, $\theta = 0.69$, $L_c = 2.8\,\text{mm}$ and tilted pulse front. $k_x = 2106\,\text{mm}^{-1}$ (black) and $k_x = 2110\,\text{mm}^{-1}$ (red).

quency components can also occur, but this is not an issue with the long chirped pulses of CPOPAs, since only one signal frequency is present at any time.

The example configurations above were based on type 1 phase matching in BBO. We also investigated type 2 phase matching, as well as the alternative materials LBO and CLBO. With type 2 phase matching we did not find any configurations with bandwidths as wide as in configuration (ii). Type 1 CLBO could offer a comparable or slightly greater bandwidth, but we choose BBO for the simulations below because its nonlinear coefficient is about three times greater than that of CLBO.

4. Simulation results

In this section, we present simulation examples for configuration (ii) of the previous section. The simulation model is based on previous work [26, 27], but it has been extended to handle broad-bandwidth beams with high accuracy. Although it works with equations for the envelopes, it does not make the slowly varying envelope approximation: The program calculates the spatial evolution of the amplitude of each spectral and angular component. The essential approximation is that the spectral amplitudes vary slowly compared to the optical wavelength. Since the rate of change of these amplitudes is determined by the gain coefficient, which is on the order of a few mm^{-1}, this approximation is well-satisfied even in high gain OPAs [28]. To save time and memory, our model takes advantage of the symmetry about the noncollinear plane ($\hat{\mathbf{x}}\hat{\mathbf{z}}$) and computes the beam spatial evolution on a single half-plane. Angularly dispersed beams are handled efficiently by factoring out the center component of the transverse spatial frequency, analogously to how the carrier frequency is factored out of the equations for the amplitudes. This allows noncollinear beams to be handled with modest spatial resolution. Because we use a transverse wavenumber (k_x and k_y) representation for the beams and a coordinate system that preserves k_x and k_y accross the interface, refraction at the crystal face is automatically taken into account by the model.

In the simulations, we modeled a 2.8 mm long BBO crystal with a peak pump intensity of 45 GW/cm^2. The temporal resolution was 2 fs and the spatial resolution was $100\,\mu$m in the critical ($\hat{\mathbf{x}}$), and $160\,\mu$m in the noncritical ($\hat{\mathbf{y}}$), directions. We verified that these resolutions were sufficient by comparing them to simulations with higher temporal or spatial resolution. We assume that the signal beam is suitably stretched and has the appropriate angular dispersion, but the stretcher and the dispersing optics are not included in the simulation. Similarly, the optics to collimate and compress the amplified beam are not included.

#3504 - $15.00 US Received 10 December 2003; revised 3 February 2004; accepted 3 February 2004

We first investigated some idealized configurations by simulating in a single transverse dimension using simulated pump and seed pulses to study the output spectra qualitatively. The seed pulse had an order-12 super-Gaussian intensity envelope of length 3 ps ($1/e^2$ full-width), shown by the black line in Fig. 7(a). It was chirped with a chirp parameter of 4×10^{-4} rad/fs^2, corresponding to a stretched-pulse spectrum ranging from 580 nm to 1300 nm (black line in Fig. 7(b)). To ensure that the whole signal pulse interacts with the same pump intensity, and to allow for temporal walk-off and the rounded corners of the pump pulse envelope, the pump was chosen to have a 5 ps long, order-12 super-Gaussian intensity envelope. The spatial distributions of both beams were super-Gaussian of order 10, with $1/e^2$ radii of 1 mm. The width of the suppressed transverse dimension was taken to be 1 mm, and the pump energy is 3.6 mJ.

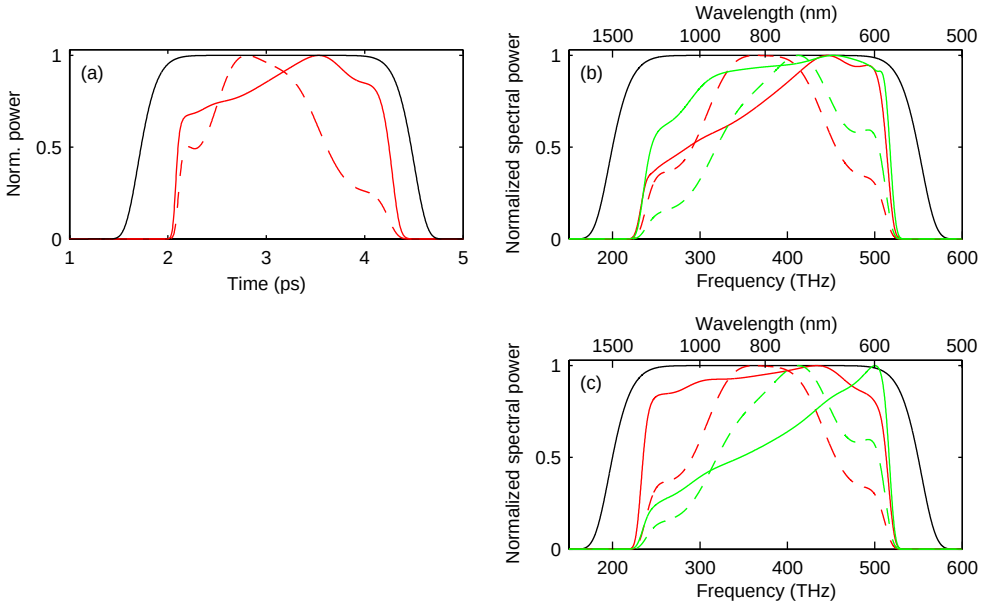

Fig. 7. (a) Normalized seed power (black) and output signals for seed intensity 10 W/cm^2 (red dashed) and 1000 W/cm^2 (red solid). (b) Spectra of seed (black), signal (red) and idler (green) for a positively chirped seed pulse. The seed intensity is 10 W/cm^2 (dashed) or 1000 W/cm^2 (solid). (c) Signal and idler spectra for a negatively chirped seed.

Figure 7(a) shows the normalized seed pulse and output signal pulses for two different seed intensities, 10 W/cm^2 (0.48 pJ, dashed lines) and 1000 W/cm^2 (48 pJ, solid lines). Figure 7(b) and (c) show the signal and idler spectra for the same two seed intensities, with positive or negative sign of the chirp, respectively. At the modest peak seed intensity of 10 W/cm^2, pump depletion is small and the amplification of the signal spectrum is approximately proportional to the gain spectrum in Fig. 6, independently of the sign of the chirp. The idler spectrum (dashed green) is skewed towards short idler wavelengths. The nonlinear interaction results in the generation of signal and idler photons in pairs; since the flat seed spectrum (solid black) comprises more low-frequency signal photons, more high-frequency idler photons are generated in the amplification process.

At a higher seed intensity of 1000 W/cm^2, the shape of the spectra is determined principally by the limiting effect of pump depletion rather than by the seed spectrum and small-signal gain. Due to the dispersive characteristics of BBO, both high and low frequency wings of the seed spectrum travel more slowly than does the central frequency (see Fig. 8) and thus experience

#3504 - $15.00 US Received 10 December 2003; revised 3 February 2004; accepted 3 February 2004

temporal walkoff relative to the pump pulse. For the seed stretched in a positive-dispersive material, the low signal frequency components in the leading edge of the pulse interact with successively later parts of the pump pulse that have already been depleted. By contrast, the high frequency trailing edge continually interacts with undepleted parts of the pump and thus experiences higher gain, which gives rise to the signal spectrum skewed towards the high frequency end (Fig. 7(b), solid red line). This mechanism works oppositely for the idler because it has the opposite chirp of the signal. If the sign of the seed chirp is reversed, the qualitative features of the signal and idler spectra at high seed power are reversed also, as shown in Fig. 7(c). The relatively flat signal spectrum in this case may be an advantage in some applications, but in the remaining examples we assume a positive seed chirp, as is common in chirped-pulse amplifiers. The output signal energy is 0.68 mJ, which corresponds to a conversion efficiency into the signal of 19%. In all cases, the amplification bandwidth exceeds one octave.

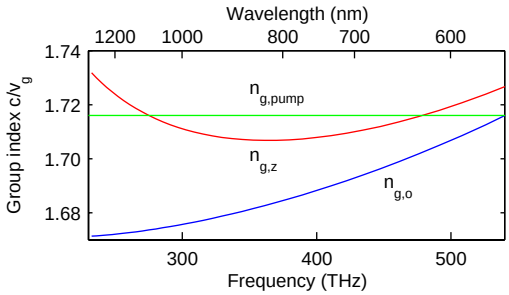

Fig. 8. Signal group velocity index as a function of frequency for configuration (ii). The blue line shows the group index for the ordinary (slow) polarization in BBO, while the red line shows the effective group index in the $\hat{\mathbf{z}}$-direction calculated using Eq. (3). The approximate symmetry of $n_{g,z}$ around the degenerate frequency (375 THz) reflects wideband phase matching. The $n_{g,3} = 1.716$ group index of the pump beam is shown by the green line.

In order to obtain a more realistic estimate for the conversion efficiency, we extended the simulation to include both transverse dimensions. We used pulses with the same parameters as above, but reduced the pump pulse duration to 4 ps to improve the conversion efficiency. Figure 9(a) shows the input and output pulse shapes. For an input pump energy of 4 mJ (45 GW/cm^2), a seed energy of 67 pJ yielded 0.82 mJ of amplified signal output This corresponds to a signal gain of 10^7 and a conversion efficiency into the signal of 20%. The input and output signal spectra, which have the same qualitative features as discussed above, are shown in Fig. 9(b).

Figure 9(c) shows the fluence distribution of the output signal beam; it is round and undistorted at this moderate conversion efficiency. The small asymmetry and offset from the model origin in the horizontal direction is due to the noncollinearity and the Poynting vector walk-off of the pump. Figure 9(d) shows the far-field in the $\hat{\mathbf{x}}$-direction as a function of wavelength for the seed and output signal. Apart from the overall change of the spectrum, the far field is well preserved in the output. This implies that the output beam has the same angular dispersion as the input beam, allowing it to be recollimated by an optical arrangement identical to that which dispersed the seed.

The spectral phase of the central spatial element of the output beam, relative to the phase of a beam that has propagated passively through the crystal, is shown in Fig. 9(e). The nonlinear mixing introduces a phase shift because of the nonzero phase-mismatch. This phase shift must be compensated for the compressed pulses to approach the transform limit, shown by the

#3504 - $15.00 US Received 10 December 2003; revised 3 February 2004; accepted 3 February 2004

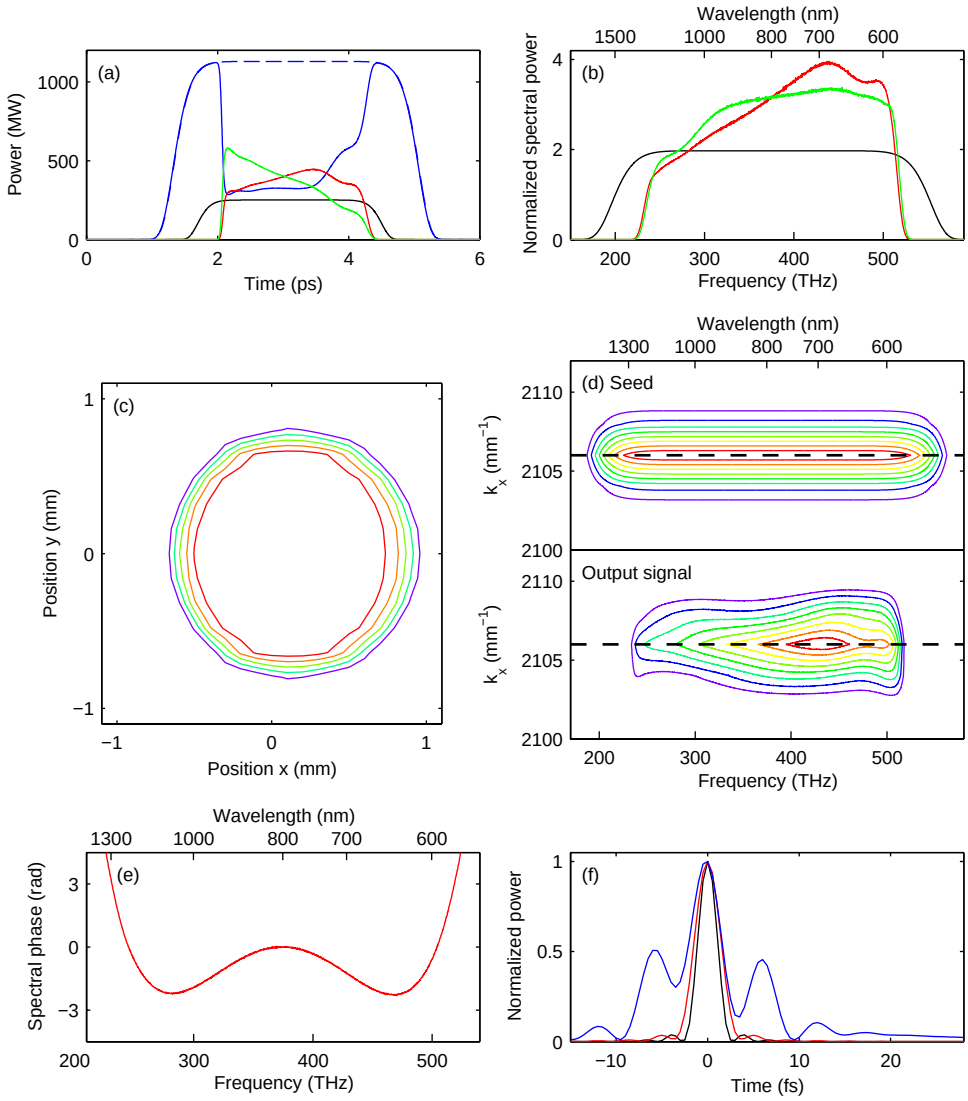

Fig. 9. Simulation results for idealized super-Gaussian beams. (a) Temporal profiles of the input pump (blue dashed), output pump (blue solid), input seed (10^7 times magnified, black), output signal (red), and idler (green). (b) Spectra of seed (10^7 times magnified, black), output signal (red), and idler (green). (c) Contours of output signal fluence distribution. (d) Far-field spectra for the $\hat{\mathbf{x}}$-direction (noncollinear direction) of the seed (upper) and output signal (lower). The dashed lines show the center k_x values. (e) Spectral phase of output signal relative to a passively propagated beam. (f) Transform limited pulses corresponding to the seed spectrum (black) and output signal spectrum (red). Their durations are 2.4 fs and 3.3 fs (FWHM), respectively. The blue curve shows the pulse corresponding to the output signal spectrum and the nonlinear phase distortion from (e).

#3504 - $15.00 US Received 10 December 2003; revised 3 February 2004; accepted 3 February 2004

red line in Fig. 9(f); if the phase is left uncompensated, the compressed pulse is longer and has significant pre- and post-pulses (blue line). For comparison, the transform limited pulse corresponding to the seed spectrum is shown by the black line. Since the spectral phase is well-behaved, we anticipate that such compensation is possible using a spectral shaper or acousto-optic dispersive filter (DAZZLER) [29].

Lastly, we exploited the full potential of the numerical simulation by modeling a measured seed pulse. We modified the pump beam to have Gaussian spatial and temporal profiles, but maintained the 1 mm $1/e^2$ waist radius and the 4 ps pulse duration (full width to $1/e^2$). The peak pump intensity was 45 GW/cm^2, as above, which corresponded to an energy of 1.7 mJ. The complex seed temporal envelope was taken from a SPIDER measurement of a real 3.8 fs (FWHM) pulse obtained by compressing the output from a hollow fiber [30]. The pulse was stretched by numerical propagation through a 10 mm block of SF5 glass, taking all dispersion orders into account, making its length comparable to that of the pump pulse. The seed beam transverse profile was Gaussian with 1 mm radius, matching that of the pump. Figure 10 shows the results. For a seed energy of 0.6 nJ we obtained 190 μJ of amplified output, which corresponds to 11% conversion efficiency. As mentioned previously, there exists some trade-off between conversion efficiency and spectral gain bandwidth in the wings of the stretched seed pulse. The seed energy in this example was chosen an order of magnitude greater than in the previous example in order to enhance conversion in the (spatial and temporal) wings of the pump pulse.

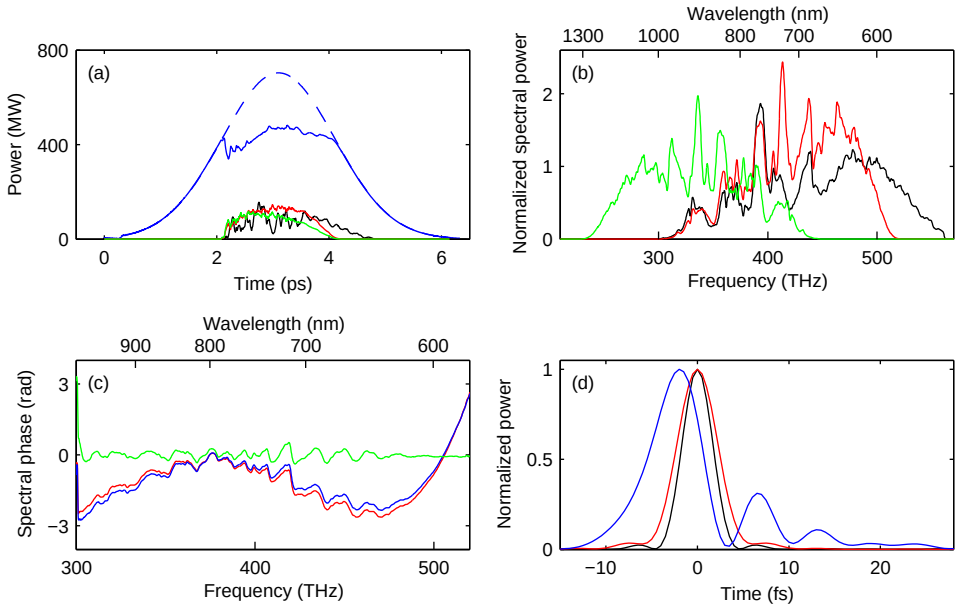

Fig. 10. Results for a measured seed pulse, Gaussian pump pulse, and Gaussian spatial profiles. (a) Temporal profiles of the input pump (blue dashed), output pump (blue solid), input seed (3×10^5 times magnified) (black), output signal (red), and idler (green). (b) Spectra of seed (3×10^5 times magnified) (black), output signal (red), and idler (green). (c) Spectral phase of output signal relative to a passively propagated beam with $n_2=0$ (red) and $n_2=10^{-15}$ cm^2/W (blue). The green curve shows the rapid part of the phase variation alone. (d) Transform limited seed (black) and signal (red) pulses. The blue curve shows the pulse corresponding to the output signal spectrum and the nonlinear phase distortion (the red line in (c)).

#3504 - $15.00 US Received 10 December 2003; revised 3 February 2004; accepted 3 February 2004

The seed spectrum, shown as the black line in Fig. 10(b), is not optimally matched to the OPA because it is centered below 800 nm and extends below 600 nm, but it is nevertheless amplified with only small spectral clipping, yielding the spectrum shown in red in Fig. 10(b). Figure 10(c) shows the spectral phase relative to a passively propagated beam. With this phase left uncompensated, the pulse shown by the blue line in Fig. 10(d) is obtained. The transform limit of the amplified spectrum (red) indicates that with these realistic parameters, the CPOPA can support pulses as short as 5.2 fs.

The slow variation in spectral phase is similar to that of the idealized pulses discussed above, but there is now some additional rapid variation. The latter could be eliminated numerically by reducing the seed power, which reduced the nonuniform pump depletion caused by the rapidly varying signal power. Compression of a pulse with only the rapid phase variations (green line in Fig. 10(c)) yields almost the transform limit, from which we conclude that the broadening of the blue pulse is primarily caused by the slow phase variation.

Including a nonlinear refractive index n_2 to investigate possible self-phase modulation, leading to additional spectral broadening, we found that the effect of n_2 was very small, and the resulting spectral phase differed only negligibly, as seen from the blue line in Fig. 10(c). The value of $n_2 = 10^{-15}\mathrm{cm}^2/\mathrm{W}$ used was a conservative estimate because it is higher than the values measured for BBO [31, 32] by a factor 2 or 3.

5. Conclusions

We have investigated broadband phase matching of a CPOPA by spectrally dispersing the seed beam. We could use the freedom of tilting the pulse fronts to match the group velocities of signal and idler, since the relatively long pulses of chirped pulse amplification alleviate the need for precisely matched pump and signal velocities using pulse-front tilting. By using this technique and considering a number of possible noncollinear phase matching configurations in BBO, we have identified one that gives an octave gain bandwidth from about 600 nm to 1200 nm when pumping at 400 nm. Detailed numerical simulations of a measured 3.8 fs seed pulse show an output spectrum of about 200 THz width, corresponding a transform limit of 5.2 fs, although the measured spectrum was poorly matched to the CPOPA gain and did not exploit the full bandwidth. With 1.7 mJ pump energy (45 GW/cm^2) and a 2.8 mm long BBO crystal, the seed pulses were amplified from 0.6 nJ to 190 μJ, corresponding to a gain of 3×10^5. Using idealized pulses, the model results showed pump depletions as high as 40%, and gains of 10^7 across the whole octave. The configuration chosen has the additional advantage that the generation of parasitic second harmonic is not phase matched.

In the simulation examples we assumed modest pump energies, which currently pose a limitation on experimental CPOPA systems. This does not represent the limit of CPOPA, whose pulse energy can be scaled by making the pulses longer or the beams wider. Such scaling has beneficial side-effects: Longer pulses reduce the influence of temporal walk-off, and wider beams make the spatial walk-off caused by the Poynting vector walkoff and noncollinearity less important. The principles of broadband phase matching by angular dispersion investigated here are quite general and can, in principle, be applied to any wavelength range, provided a suitable combination of nonlinear crystal and pump can be found.

Acknowledgments

We thank Gunnar Rustad for useful comments.

#3504 - $15.00 US Received 10 December 2003; revised 3 February 2004; accepted 3 February 2004